ADVANCED FUNCTIONAL MATERIALS
www.afm-journal.de

Magnetic, Multilayered Nanotubes of Low Aspect Ratios for Liquid Suspensions

Robert Zierold, Zhenyu Wu, Johannes Biskupek, Ute Kaiser, Julien Bachmann, Carl E. Krill III, and Kornelius Nielsch*

This work presents a synthesis route for low-aspect-ratio nanotubes consisting of a layer of magnetite (Fe_3O_4) sandwiched between SiO_2 layers. In this template-based strategy, self-ordered porous alumina membranes are combined with the atomic layer deposition of SiO_2 and Fe_2O_3. An optimized electrochemical setup yields nanoporous Al_2O_3 membranes on 4-inch Al substrates, which serve as templates for the large-scale fabrication of nanotubes. A selective chemical etching step releases the magnetic tubes for suspension in a carrier fluid and permits recycling of the underlying aluminum foils for the fabrication of subsequent nanotube batches. The nanotubes consisting of an iron oxide layer protected by a silica shell are magnetically characterized in suspensions as well as in dried form on a substrate. High-resolution transmission electron imaging reveals a polycrystalline, magnetite spinel structure of iron oxide, with the proper stoichiometry proven by the presence of the Verwey transition. Furthermore, field-dependent viscosity measurements show an enhancement of the magnetoviscosity, thus demonstrating the technological potential of nanotube suspensions as a new class of ferrofluidic solutions. Owing to the tubular shape being closed at one end, these nanoparticles might additionally function as magnetic containers for targeted drug-delivery or as chemical nanoreactors.

1. Introduction

The magnetic properties of geometrically confined objects depend on their sizes and shapes, and the extent to which such microscopic characteristics translate into phenomena observable at the macroscopic scale—such as in magnetic suspensions—depends on two conditions. Firstly, a sufficient large number or concentration of magnetic nanoobjects must be achieved and, secondly, these objects must manifest narrow size and shape distributions. Inorganic magnetic nanoparticles (NPs) can fulfill both of these requirements, which makes them nearly ideally suited to application in liquid suspensions. However, magnetic NPs are restricted in terms of the available shapes. Wet-chemical syntheses based on the thermal decomposition of precursor molecules, sol-gel routes, and aerosol-based approaches all impart the flexibility to tailor the average particle size over three orders of magnitude while (sometimes) maintaining a narrow size distribution, but the particle shapes are generally limited to being spherical or cubic.[1,2] Such colloid synthesis techniques can be adapted to the preparation of rod-like particles, but control of the length, diameter, or shape turns out to be challenging because of the high sensitivity to growth conditions.[3–5]

As an alternative, elongated nanostructures can be prepared by the vapor-liquid-solid (VLS) growth mechanism, often using a catalyst droplet as nucleation seed.[6–8] The VLS method is best known for the preparation of semiconductors and metal oxides, whereas magnetic particles have been achieved only in a few cases, either by doping with transition metal ions,[9–11] or in the unique case of ferrites where the growth was assisted by pulsed laser deposition.[12]

Besides the previously described synthesis routes, template-assisted synthesis strategies offer much greater control over the shape of the magnetic objects—at the cost of the overall mass yield being limited by the available template area.[13] Commonly employed template-based approaches are carried out on anodic aluminum oxide (AAO), porous silicon, electrochemically synthesized TiO_2 tubes, self-assembled block-copolymers, nuclear ion track-etched membranes, or Tobacco mosaic virus particles; in all cases, a mold, mask, or guide controls the deposition of the magnetic particles, and several growth methods can be used, including electrodeposition, electroless deposition, and chemical or physical vapor deposition.[14–18]

In the case of AAO membranes, the pores of the template determine the geometry, size distribution, and local ordering of the synthesized particles. The combination of AAO membranes with atomic layer deposition (ALD), as a thin-film deposition

R. Zierold, Prof. J. Bachmann, Prof. K. Nielsch
Institute of Applied Physics
University of Hamburg
Jungiusstraße 11, 20355 Hamburg, Germany
E-mail: rzierold@physnet.uni-hamburg.de
Z. Wu, C. E. Krill III
Institute of Micro and Nanomaterials
Ulm University
Albert-Einstein-Allee 47
89081 Ulm, Germany
Dr. J. Biskupek, Prof. U. Kaiser
Central Facility of Electron Microscopy
Ulm University
Albert-Einstein-Allee 11
89081 Ulm, Germany

DOI: 10.1002/adfm.201001395

technique, results in nanotubes embedded in the Al_2O_3 matrix.[19] ALD is especially suited to the conformal coating of the pore walls because of its self-limiting nature: the deposition of material during ALD is based on sequential chemical reactions occurring at the sample surface, implying that growth is not controlled by the local rate of mass transport of the gaseous molecular precursors.[20] The atomic layer deposition of magnetic material onto porous AAO puts the experimentalist in control of all parameters that are relevant to the magnetic behavior of individual nanotubes: the tube length and diameter are determined by the template, whereas the wall thickness and the material in question depend on the applied ALD procedure.[21] Furthermore, the capability of preparing multilayers of magnetic and non-magnetic materials in porous alumina substrates by ALD makes it possible to synthesize samples for transmission electron microscopy of released magnetic tubes,[21] to insulate magnetic tube walls for further electrodeposition of a magnetic core,[22] and to study structural and magnetic properties as a function of growth conditions.[23]

The synthesis, physical characterization, and theoretical modeling of magnetic suspensions of spherical NPs—so-called ferrofluids—have been researched for more than forty years.[24–26] In particular, the magnetic field-induced formation of chain-like aggregates of NPs can lead to an enhancement of the ferrofluidic viscosity by up to two orders of magnitude. However, at elevated shear rates the interaction holding the nanoparticle chains together can be overcome and a dramatic viscosity decrease is observed. Replacement of the spherical nanoparticles of conventional ferrofluids by rigid elongated nanorods may circumvent this viscosity drop at higher shear rates.[27] The colloidal behavior of elongated solid nanowires suspended in a carrier liquid as well as their individual behavior has already been investigated.[28,29] On the one hand, liquid suspensions of magnetic particles have found technological application in magnetic seals,[30] lithography masks,[31] and damping systems.[32] On the other hand, magnetic nanoparticles—especially iron oxide-based systems—have been investigated for biomedical applications,[33,34] such as cancer therapy and diagnostics,[35] medical imaging contrast agents,[36] or drug carriers.[37] Among the more exotic uses of magnetic objects in the medical field are cell separation,[38] gene delivery,[39] and mechanical cell destruction by means of magnetic vortices in microdiscs.[40]

In this paper, we report the preparation of anisotropic magnetic particles according to a template-based strategy with high scale-up potential. A substrate recycling step enables reuse of the high-purity aluminum starting material in a closed preparative cycle. Multilayered tubular, magnetic nanoobjects can thus be produced in sufficient quantities for macroscopic volumes of a liquid suspension, for which improved magnetoviscous properties can be expected. The tubular shape of the nanomagnets differentiates these suspensions from conventional ferrofluids, and the change in particle shape might lead to new applications for magnetic suspensions.

2. Results and Discussion

2.1. Preparation

Our overall approach to the synthesis of magnetic, multilayered nanotubes having low and accurately tunable aspect ratios and to their subsequent suspension in a carrier liquid is displayed in **Scheme 1**. The porous alumina template is prepared by a two-step anodization procedure[41] applied to an aluminum foil followed by wet chemical etching to widen the pores. Subsequent sequential ALD processes, reactive ion etching (RIE) steps, and thermal reduction results in magnetic nanotubes embedded in an alumina matrix. Selective etching of the template releases the magnetic nanotubes into an acidic suspension and allows for recycling of the underlying aluminum substrate. Transfer of the suspended nanoparticles to a pH-neutral liquid medium prepares them for magnetic field-dependent viscosity characterization.

Detailed control of the aspect ratio (between 1 and 10) is realized by the parameters chosen for the second anodization step.[42] In order to permit fine adjustments of the pore length (the length of the future nanotubes), the overall charge density passed through the system during electrochemical oxidation is controlled accurately. Cross-sectional scanning electron microscopy (SEM) images of the porous membranes (**Figure 1**a,b) and transmission electron microscopy (TEM) images (Figure S1 in the Supporting Information) of released tubes provide evidence for a linear relationship between the pore depth and the transported charge (Figure 1c). The slope in Figure 1c, which is proportional to the growth rate of the pore length, amounts to 417 (±7) nm cm^2 C^{-1}. At this point, the pore diameter of the alumina membrane amounts to 38 (±2) nm and directly corresponds to the diameter of the nanotube body (Figure S1). Isotropic chemical etching (Scheme 1b) widens the pores laterally and removes the nail-head structure of the prepared tubes (highlighted in red in Figure S1 in the Supporting Information). A silicon dioxide layer is deposited onto the pore walls[43] as a

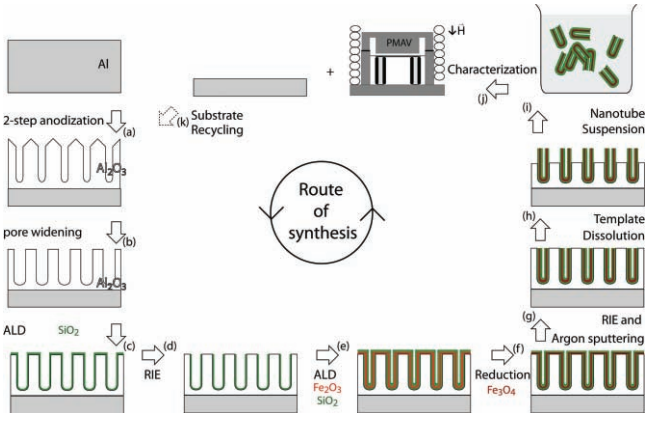

Scheme 1. Schematic presentation of the synthesis path for the preparation of a magnetic nanotube suspension. a) An electropolished aluminum plate is anodized twice, whereby the second anodization is carried out in a highly controlled manner to establish the tube length. b) Pore widening helps to remove the conical top structure of the membrane. c) In a first ALD process SiO_2 is deposited. d,e) Subsequently, the interconnects are removed by a reactive ion etching step (d), followed by deposition of iron oxide and silica (e). f,g) The iron oxide is reduced to magnetite (f) and the connecting top layer is removed via RIE and argon sputtering (g). h–j) The supporting template is dissolved (h), followed by a washing procedure that results in a nanotube suspension (i) ready for characterization (j). k) The underlying substrate is recycled and the next cycle starts without having to repeat the electropolishing and first anodization steps.

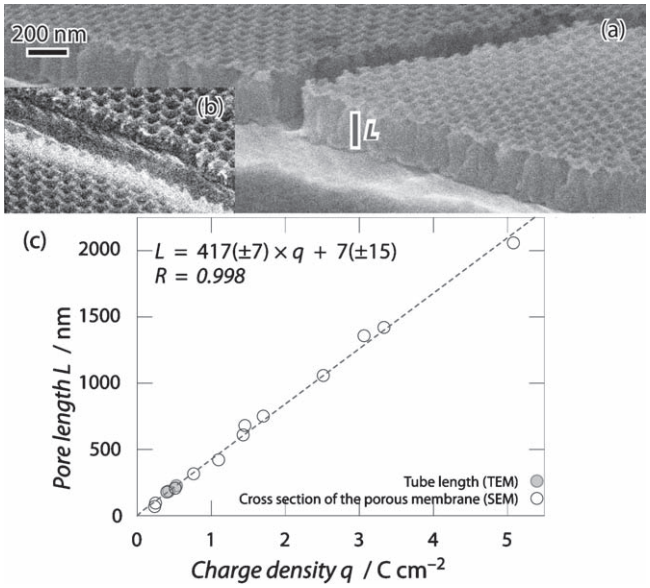

Figure 1. a,b) Exemplary cross-sectional views of porous alumina membranes as recorded by scanning electron microscopy. From such images the pore lengths plotted in (c) were determined (open circles). The pore length was found to scale linearly with the charge density that is transported during the second anodization process. The gray circles show the length of tubes released, and measured by TEM after all synthesis steps without pore widening (Figure S1).

protective outer layer of the tubes (Scheme 1c). At this point, a silica layer is also present on the top side of the alumina membrane, thereby connecting the embedded tubes to each other. These interconnects are selectively removed by anisotropic reactive ion etching (RIE) (Scheme 1d). ALD is used to coat the resulting sample with iron(III)oxide and by a second layer of SiO_2 in order to achieve the final multilayer wall structure (Scheme 1e). Thermal reduction of Fe_2O_3 in argon-hydrogen atmosphere results in conversion to the magnetic iron(II,III) oxide (Fe_3O_4) phase.[44] At this point, the tubes are once again connected by layers of iron oxide and SiO_2 that were deposited subsequent to reactive ion etching. Thus, RIE is conducted once again to remove the interconnects (Scheme 1g). In this manner, each single tube is separated from its neighbors—a crucial prerequisite for a complete dispersion of the nanotubes into the carrier solvent in the subsequent step. The latter is performed by selective chemical dissolution of the supporting alumina matrix in chromic acid (Scheme 1h), whereby a surrounding silica shell protects the magnetic layer of each nanotube against etching. The tubes are released into the acidic solution and the underlying aluminum substrate is separated. The suspension is sonicated briefly, then filtered, and washed several times (Scheme 1i) until the carrier liquid is pure water. Finally, the suspension of nanotubes is ready for further characterization.

Structural investigations as well as physical measurements were carried out on nanotubes with an average length of 190 (±10) nm and a mean tube diameter of 90 (±5) nm. These values correspond to the geometry that is expected after the applied wet chemical pore widening. The three-layer structure of the SiO_2-Fe_3O_4-SiO_2 nanotube wall is apparent in aberration-corrected high-resolution transmission electron (AC-HRTEM) images of a dried nanotube suspension (**Figure 2**a). The thicknesses of the inner and outer silicon oxide layers and the magnetic layer amount to 6 (±1) nm and 8 (±2) nm, respectively, as can be seen in the inset of Figure 2a. The continuous silica shells are evident, as they remain amorphous after heat treatment. In contrast, the confined iron oxide layer features a polycrystalline microstructure, which is obvious at high magnification (Figure 2b) by the various orientations of crystal planes. Additionally, the diffraction rings in the selected area electron diffraction (SAED) pattern of a tube ensemble (Figure 2d) and the fast Fourier transform of a HRTEM image of a single tube. as shown in the Supporting Information (Figure S2), confirm the polycrystalline spinel magnetite phase. This is consistent with grazing-incidence X-ray diffraction (GIXRD) data (Figure S3).

The well-defined iron oxide layer and the homogeneous distribution of iron atoms along the entire length of the tubes is evident from the images in Figure 2c, which were recorded by high-angle annular dark-field (HAADF) scanning TEM imaging. The narrow distribution in nanotube length and size is apparent from the left image of Figure 2c, and the higher-magnification view (Figure 2c, right image) reveals the presence of minor voids in the iron oxide layer, which could originate from a volume decrease during the reduction step caused by the partial removal of oxygen atoms.

2.2. Recycling and Scale-Up

The aluminum substrate is not attacked by the chromic acid etch used to release the nanotubes. Furthermore, it retains a record of the long-range order of the former nanoporous structure in the form of concave hemispheres located at the positions of the Al_2O_3 pore extremities. These hemispherical indentations act as new nucleation sites for pore growth during subsequent anodization.[41] In light of this fact, the aluminum template can be recycled and immediately inserted into Scheme 1 at the second anodization step (Scheme 1k). Not only does this approach save resources but also a significant amount of time entailed by having to electropolish the aluminum substrate and initiate pore nucleation during the first anodization step (at least 20 h). Scale-up of this template-based synthesis has become economically feasible.

For scale-up, the anodization setup had to be enlarged to handle aluminum foils with an area of approximately 54 cm^2 (diameter 8.3 cm), implying the flow of electrical currents in excess of 10 A during electropolishing as well as 150 mA during anodization—along with corresponding Joule heating. The cathode of the scaled-up system consisted of a 0.5 mm thick Ag wire (as replacement for the standard Pt mesh), which could support the large current densities delivered by $Pb/Pb(SO_4)_2$ batteries. The heat generated at the sample was dissipated by a 2-kW cooling circuit. Additionally, the surface ratio between the anode and cathode was increased from 1/8 to 1/3 for the scaled-up system. The outstanding deposition homogeneity that we achieved over a large surface area by ALD enabled the single-batch synthesis of more than six hundred billion (6×10^{11}) nanotubes identical in diameter, length, and wall thickness at a time. Thermal reduction of the tubes (still attached to the template) was carried out in a stainless steel vessel placed on a hot plate at a temperature of 400 °C.

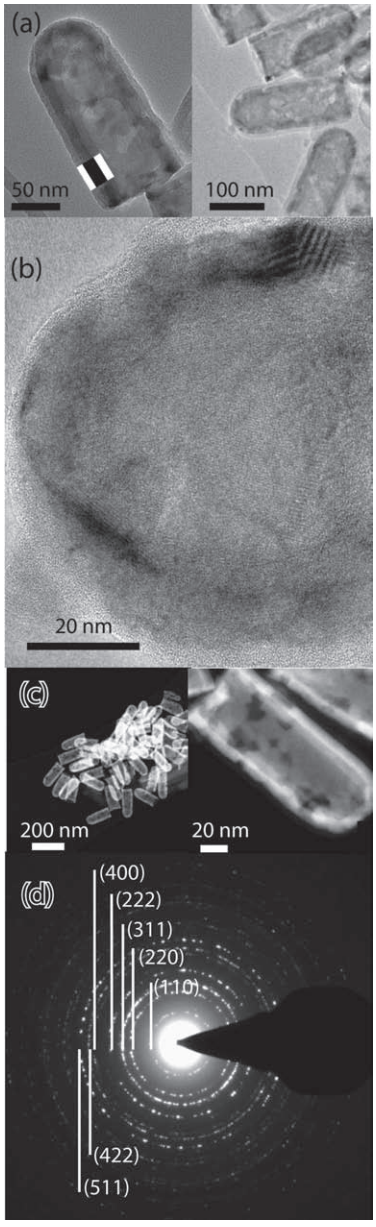

Figure 2. High-resolution transmission electron microscopy images of a) nanotubes showing the well-defined, three-layered wall structure consisting of silica (highlighted in white) and iron oxide (black) (tube length 180 nm, diameter 90 nm, thickness of each silica layer 6 nm, iron oxide thickness 8 nm). The iron oxide is polycrystalline but the silica layers remain amorphous (magnified HRTEM of a single tube in (b)). The narrow distribution of tube lengths and diameters as well as the homogeneous distribution of iron in the iron oxide layer are apparent in the high-angle annular dark-field scanning TEM images presented in (c). Magnification of a single tube shows small voids in the magnetic layer, which are probably caused by volume shrinkage during the reduction step. d) Polycrystalline magnetite can be identified by electron diffraction in which all rings correspond to iron(II,III)oxide (Fe_3O_4).

2.3. Physical Characterization

Superconducting quantum interference device (SQUID) magnetometry measurements performed on a dried nanotube suspension placed on a flat silicon substrate are displayed in **Figure 3**. Here, magnetization isotherms are shown for two temperatures (5 K and 300 K) in two different alignments of the substrate plane relative to the applied magnetic field. The in-plane and out-of-plane configurations (Figure 3a and 3b) refer to the applied magnetic field being oriented in the plane of the silicon substrate and perpendicular to it, respectively. A non-zero coercive field and remanent state are observable in both configurations at 5 K as well as at 300 K. The coercivity at 5 K was 910 Oe in the in-plane configuration, whereas the out-of-plane measurement (in which the field is perpendicular to the long axis of most tubes) yielded a reduced value of 690 Oe at the same temperature. Similar behavior was found when comparing the remanent magnetization (normalized to the saturation magnetization) in the two directions. At 5 K, the in-plane value of 55% dropped to 35% in the out-of-plane configuration. Furthermore, raising the measurement temperature to 300 K lowered the magnitude of coercivity and remanence, but it did not change the general decrease in values for the coercive field (270 Oe/160 Oe) and remanent magnetization (35%/20%) between the in-plane and out-of-plane configurations. These observations define that the magnetic easy axis of our anisotropic structures lies along the long axis, as expected.

Temperature-dependent zero-field-cooled measurements (warm-up mode) performed at a permanent applied field of 600 Oe (Figure 3c) and in remanence after saturation at 10 kOe (Figure S3 in Supporting Information) display a step between 95 K and 125 K in a plot of the magnetic moment versus temperature. This obvious change in curve progression is associated with the Verwey transition of magnetite.[45] Accordingly, the derivative of the magnetic moment versus the temperature is plotted in the same figure as gray, hollow circles. The location of the peak characterizes the Verwey temperature for the corresponding phase transition. The measured value of T_v = 107 K is lower than that for the bulk material (T_v around 125 K).[46] This observation agrees with previous studies for thin films[47] and electrodeposited nanowires,[48] for which similarly reduced transition temperatures were reported as well. The observed transition is an additional evidence for the stoichiometry of Fe_3O_4 in the iron oxide layer of our nanotubes, as no Verwey transition occurs in the gamma phase of Fe_2O_3, maghemite. To our knowledge, this is the first time that the Verwey transition has been observed in iron oxide films deposited by ALD.

Implementation of the scaled-up synthesis described above enables the transfer of the magnetic properties of nanotubes embedded in a template to a liquid suspension. **Figure 4a** shows a photograph of a well-dispersed magnetic nanotube suspension in an Eppendorf tube. Applying a strong external magnetic field collects the tubes near the magnet, leaving the remainder of the solvent transparent. After removing the magnet and shaking the suspension, the latter reverts to the initial, well-dispersed state.

In contrast to the hysteresis curves recorded for dried nanotubes, the liquid suspension of Figure 4b manifests a zero crossing in the magnetization isotherm at room temperature, which highlights a qualitative difference in the collective magnetic properties of fixed tubes and those suspended in a liquid. The vanishing remanent magnetization and coercive field substantiate the idea of well-separated particles able to rotate. In

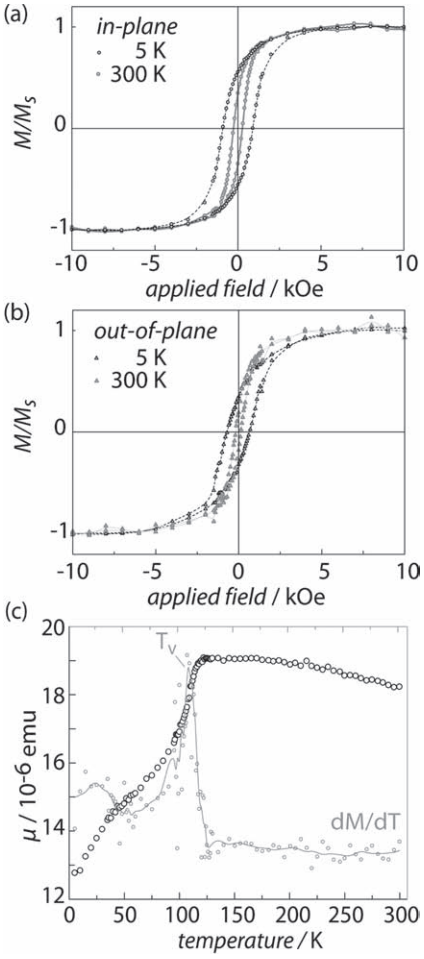

Figure 3. a,b) Magnetization isotherms recorded at 5 K (black symbols) and 300 K (gray) for a dried nanotube suspension mounted in a SQUID magnetometer in (a) in-plane and (b) out-of-plane configurations. Reduced values of coercivity and remanent magnetization in the out-of-plane configuration supports the conclusion that the easy-axis of magnetization lies parallel to the long axis of each nanotube. In (c) the magnetic moment measured in an applied magnetic field of 600 Oe is plotted in black, open circles as a function of temperature. To emphasize the sharp increase between 95 K and 125 K the derivative of the magnetization with respect to the temperature is plotted in gray circles. The peak observable at 107 K (T_V) is associated with the Verwey transition of magnetite. All lines drawn serve as guides to the eye.

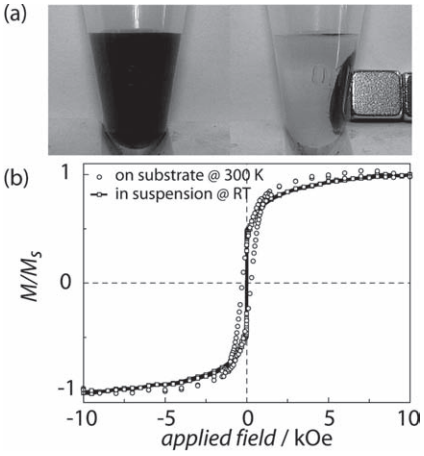

Figure 4. a) The left photograph in shows a well-dispersed suspension of magnetic nanotubes in a liquid. In the magnetic field gradient of a permanent magnet (right image) the tubes are collected in the vicinity of the magnet, leaving the remainder of the solvent transparent. b) Magnetization isotherms (magnetic moment normalized to the saturation magnetization) for tubes dried on a substrate (open circles) and liquid suspension of nanotubes (open squares with lines). The coercive field and remanence of the suspension are both zero, as expected for nanotubes that are free to rotate. The line serves as guide to the eye.

comparison to superparamagnetism, in which thermal energy causes a rapid change in orientation of the magnetic moments within a particle, the majority of the magnetic moments within our nanotubes is fixed in direction, but the tubular particle itself is able to move and rotate. Thereby, the magnetization direction imposed by an external magnetic field is lost in the zero-field state.

Viscosity measurements of the nanotube suspension—performed with a piezo-membrane axial vibrator (PMAV) equipped with a magnetic coil—are shown in **Figure 5**b. The PMAV measurement system is based on a membrane vibrating with an adjustable frequency actuated by piezoelectric elements, which results in a cyclic squeeze-flow of a liquid sample in contact with the membrane (and held in place on the opposite side by a parallel plate) (Figure 5a). The response of the overall system (sample and PMAV) is detected by a piezoelectric sensor via a lock-in amplifier and converted into the complex elasticity modulus, from which the complex viscosity of the sample is determined after removing the instrumental contribution.[49,50] The magnetoviscosity can be quantified as the viscosity increase of the suspension in an applied magnetic field at a certain vibrating frequency, normalized to the viscosity in zero field,

$$\text{magnetoviscosity} = \frac{\Delta\eta}{\eta} = \frac{\eta_B - \eta_0}{\eta_0} \quad (1)$$

The magnetic concentration of the measured magnetic nanotube suspension amounted to 0.055 emu mL^{-1}, from which we estimated a volume fraction of iron oxide in the suspension of 0.02 vol% assuming a saturation magnetization of 320 emu mL^{-1} at room temperature. The latter value takes into account the measured decrease in saturation magnetization of iron oxide upon reduction of the sample size into the nanometer range.[51,52] At a constant shear frequency of 10 Hz, the magnetoviscosity was observed to increase as a function of the applied magnetic field to a value of 65% at 110 mT (Figure 5b). The nonlinear, saturating curve shape of the magnetoviscosity, which was theoretically derived by Shliomis,[53] occurred in the same field range (>100 mT) as was observed for saturation of the magnetization isotherms of the liquid suspension. Additional viscosity measurements performed at a constant applied magnetic field (45 mT) exhibited a nonlinear decrease in the magnetoviscosity as a function of the frequency—an example of the shear-thinning effect.[54,55] It is remarkable that even at a magnetic volume fraction of only 0.02 vol% a significant magnetoviscosity could be measured, comparable to the values obtained for a magnetic nanorod suspension, as reported by Birringer et al. in 2008.[27]

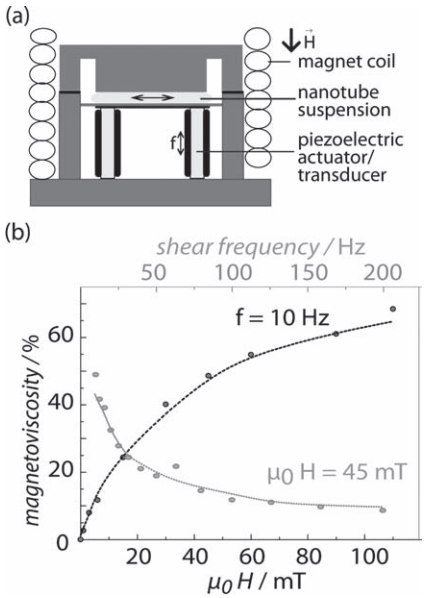

Figure 5. a) Schematic setup of the piezo-membrane axial vibrator (PMAV) used to measure the viscosity of liquid suspensions as a function of an applied axial magnetic field. b) Magnetoviscosity of a nanotube suspension as a function of magnetic field (bottom axis) at a constant vibrational frequency *f* of 10 Hz. The gray circles depict the nonlinear decrease in magnetoviscosity as a function of vibrational frequency (top axis) at a constant applied magnetic field of 45 mT. The lines drawn serve as guide to the eyes.

3. Conclusions

In this work we have demonstrated a template-based synthesis route for preparing novel, multilayered magnetic nanotubes for suspension in liquids. Scale-up of the anodization setup and development of a substrate recycling scheme make the large-scale production both economically feasible and fast enough for the preparation of macroscopic sample volumes. All processes used in the synthesis route—namely anodization, ALD, and RIE—are state-of-the-art on the industrial level for surface passivation and semiconductor processing. Structural analysis of the nanotubes revealed the presence of a polycrystalline iron oxide layer embedded between amorphous silica layers. Magnetic measurements performed on ensembles of tubes dried on a substrate were consistent with the magnetization isotherms expected for ferrimagnetic iron oxide. Furthermore, temperature-dependent measurements proved the correct stoichiometry of magnetite by direct observation of the Verwey transition. Liquid suspensions of the nanotubes manifested a vanishing coercivity and remanence as a function of the applied magnetic field, which was in good agreement with the behavior expected for rotationally free tubes. Additionally, viscosity measurements performed in various external fields exhibited a response in form of a viscosity increase.

Further improvements of the long-term stability of the magnetic suspensions against aggregation and sedimentation as well as detailed comparisons of the magnetoviscosity of nanotube suspensions with that of conventional ferrofluids are needed to gain physical insight into the solution behavior of the magnetic nanotubes. These novel magnetic nanotube suspensions could lead to a new class of ferrofluids. Alternatively, the biocompatibility of their constituent materials allows for their use as drug carriers. Additionally, the inner and outer silica surfaces have the unique property of being selectively functionalizable during synthesis.

4. Experimental Section

Preparation of the Nanotube Suspension: After cleaning in ethanol and isopropanol, aluminum chips (99.999% from Goodfellow) were electropolished in a mixture of 70% perchloric acid and ethanol (volume ratio 1:4) at 20 V for small Al chips (up to a diameter of 3.5 cm) and 24 V (two Panasonic motorcycle batteries each 12 V with a capacity of 12 Ah in series) for Al chips with a diameter of 8.3 cm for 5 min. The two anodization steps were carried out in 0.3 M oxalic acid at a bath temperature of 8 °C controlled by a ThermoScientific Haake PhoenixII P1–25P chiller. A potential of 40 V was applied for at least 20 h for the first anodization and it was time/charge controlled for the second one. Pore widening was performed in 5 wt% H_3PO_4 at 45 °C in a standard oven resulting in an etching rate of 2 nm min^{-1}. The porous substrate was covered in a home-made ALD reactor with SiO_2 by reaction of 3-aminopropyltriethoxysilane (heated to 100 °C), water (at 40 ° C), and ozone (at RT) at a chamber temperature of 180 °C. Iron oxide was deposited by sequential pulses of ferrocene (at 100 °C) and ozone (at RT) at a reaction temperature of 230 °C. Both processes were run with a permanent nitrogen flow of 20 sccm. Then, reduction of the iron(III) oxide into the magnetite phase was realized at 400 °C in a previously evacuated stainless steel vessel under an argon(95)-hydrogen(5) flow of 200 sccm. Both silica layers were etched in a SENTECH SI200 reactive ion etcher by CHF_3 plasma (25 sccm CHF_3 flow, 15 mTorr, 75 W). Removal of the iron oxide layer was conducted in an argon-sputter process in the same machine (10 sccm Ar flow, 10 mTorr, 200 W). The alumina matrix was dissolved in 0.18 M chromic acid at 50 °C under permanent stirring for at least 10 h. Ultrasonication helped to detach the single tubes and suspend them in the acid. Filtration was performed by using Whatman polycarbonate cyclopore ion track-etched membranes with a pore diameter of 0.2 μm. The filter membrane was then rolled up and placed in a 2 mL Eppendorf tube filled with de-ionized (DI)-water. Ultrasonication (for approx. 10 min) released the tubes from the filter membrane. Centrifugation at 13400 rpm for 30 min settled down all tubes and enabled the replacement of the supernatant by fresh DI-water. TEM samples as well as the dried nanotubes for magnetic measurements were produced by putting a droplet of the nanotube suspension on the TEM grids or on 250 μm thick silicon wafers, respectively, and letting the solvent evaporate.

Measurement Methods: Scanning electron microscopy images were recorded using Zeiss Evo50 and Zeiss Supra55 microscopes. The charge density was determined by time integration of the current transported during the anodization, normalized to the anodized surface area. Conventional transmission electron microscopy (TEM) was performed in a Philips EM 301 TEM at an accelerating voltage of 80 kV. High-resolution TEM images and selective-area diffraction patterns were acquired on a FEI Titan 80–300 TEM (300 kV operating voltage, equipped with CEOS imaging corrector for HRTEM and a Fischione HAADF detector for STEM). GIXRD was performed on a Siemens D500 diffractometer using Cu Kα radiation. The magnetic measurements of tube ensembles were carried out in a Quantum Design MPMS2 superconducting quantum interference device (SQUID) system between –10 kOe and +10 kOe at temperatures of 5 K or 300 K. Magnetization isotherms of the liquid suspension were recorded in a LakeShore vibrating sample magnetometer between –10 kOe and +10 kOe at room temperature. In all SQUID magnetization isotherm measurements the background signal of the silicon substrate was subtracted. The coercive field was estimated from the linear curve progression around the field axis to determine the point at which the magnetic moment is zero: the average of the field magnitudes determined in the forward and backward

directions of the hysteresis curve was taken to be the coercive field. The magnetoviscosity was measured in a piezo-membrane axial vibrator (PMAV, IdM Ulm, Germany) at a constant temperature of 293 K. In the PMAV, the liquid sample was confined between two horizontal plates (Ø 20 mm), the lower of which was forced to vibrate (amplitude ca. 5 nm) by a piezoelectric actuator at driving frequencies between 8 and 200 Hz. By means of an electromagnetic coil, the sample was subjected to axial magnetic fields as strong as 110 mT.

Supporting Information

Supporting Information (including the Figures labeled S1–S4) is available from the Wiley Online Library or from the author.

Acknowledgements

We gratefully thank Reinhold Meissner for essential technical help and Stephan Martens for development of the ALD controlling software. This work was supported by the German Research Council (DFG) in the framework of the priority program SPP1165 (Nanowires and Nanotubes—From Controlled Synthesis to Function) and EC Nanotechnology in Medicine (NAME).

Received: July 12, 2010
Published online: October 1, 2010

[1] A. S. Teja, P. Y. Koh, *Prog. Cryst. Growth Charact. Mater.* **2009**, *55*, 22.
[2] A. H. Lu, E. L. Salabas, F. Schuth, *Angew. Chem. Int. Ed.* **2007**, *46*, 1222.
[3] N. Cordente, M. Respaud, F. Senocq, M. J. Casanove, C. Amiens, B. Chaudret, *Nano Lett.* **2001**, *1*, 565.
[4] S. J. Park, S. Kim, S. Lee, Z. G. Khim, K. Char, T. Hyeon, *J. Am. Chem. Soc.* **2000**, *122*, 8581.
[5] L. Liu, H. Z. Kou, W. L. Mo, H. J. Liu, Y. Q. Wang, *J. Phys. Chem. B* **2006**, *110*, 15218.
[6] R. S. Wagner, W. C. Ellis, *Appl. Phys. Lett.* **1964**, *4*, 89.
[7] K. W. Kolasinski, *Curr. Opin. Solid State Mater. Sci.* **2006**, *10*, 182.
[8] N. Wang, Y. Cai, R. Q. Zhang, *Mater. Sci. Eng.: R: Rep.* **2008**, *60*, 1.
[9] U. Philipose, S. V. Nair, S. Trudel, C. F. de Souza, S. Aouba, R. H. Hill, H. E. Ruda, *Appl. Phys. Lett.* **2006**, *88*, 263101.
[10] M. Y. Lu, L. J. Chen, W. J. Mai, Z. L. Wang, *Appl. Phys. Lett.* **2008**, *93*, 242503.
[11] J. J. Cha, J. R. Williams, D. S. Kong, S. Meister, H. L. Peng, A. J. Bestwick, P. Gallagher, D. Goldhaber-Gordon, Y. Cui, *Nano Lett.* **2010**, *10*, 1076.
[12] J. R. Morber, Y. Ding, M. S. Haluska, Y. Li, P. Liu, Z. L. Wang, R. L. Snyder, *J. Phys. Chem. B* **2006**, *110*, 21672.
[13] C. R. Martin, *Science* **1994**, *266*, 1961.
[14] S. Anandakumar, V. S. Rani, B. P. Rao, S. S. Yoon, J. R. Jeong, C. Kim, *IEEE Trans. Magn.* **2009**, *45*, 4063.
[15] J. M. Garcia, A. Asenjo, J. Velazquez, D. Garcia, M. Vazquez, P. Aranda, E. Ruiz-Hitzky, *J. Appl. Phys.* **1999**, *85*, 5480.
[16] T. M. Whitney, J. S. Jiang, P. C. Searson, C. L. Chien, *Science* **1993**, *261*, 1316.
[17] S. Aravamudhan, K. Luongo, P. Poddar, H. Srikanth, S. Bhansali, *Appl. Phys. A: Mater. Sci. Process.* **2007**, *87*, 773.
[18] V. M. Prida, M. Hernandez-Velez, K. R. Pirota, A. Menendez, M. Vazquez, *Nanotechnology* **2005**, *16*, 2696.
[19] M. S. Sander, M. J. Cote, W. Gu, B. M. Kile, C. P. Tripp, *Adv. Mater.* **2004**, *16*, 2052.
[20] R. L. Puurunen, *J. Appl. Phys.* **2005**, *97*, 1213011.
[21] M. Daub, M. Knez, U. Gösele, K. Nielsch, *J. Appl. Phys.* **2007**, *101*, 09J1111.
[22] Y. T. Chong, D. Gorlitz, S. Martens, M. Y. E. Yau, S. Allende, J. Bachmann, K. Nielsch, *Adv. Mater.* **2010**, *22*, 2435.
[23] I. L. Soroka, M. Rooth, J. Lu, M. Boman, P. Svedlindh, J. O. Carlsson, A. Harsta, *J. Appl. Phys.* **2009**, *106*, 084313.
[24] S. W. Charles, *Ferrofluids–Magnetically Controllable Fluids and Their Applications* (Ed.: S. Odenbach), Vol.*594*, Springer, Berlin **2002**, pp. 3–18.
[25] R. E. Rosensweig, *Annu. Rev. Fluid Mech.* **1987**, *19*, 437.
[26] S. Odenbach, *J. Phys.: Condens. Matter* **2004**, *16*, R1135.
[27] R. Birringer, H. Wolf, C. Lang, A. Tschöpe, A. Michels, *Z. Phys. Chem.* **2008**, *222*, 229.
[28] M. Chen, L. Sun, J. E. Bonevich, D. H. Reich, C. L. Chien, P. C. Searson, *Appl. Phys. Lett.* **2003**, *82*, 3310.
[29] M. Tanase, D. M. Silevitch, A. Hultgren, L. A. Bauer, P. C. Searson, G. J. Meyer, D. H. Reich, *J. Appl. Phys.* **2002**, *91*, 8549.
[30] B. M. Berkovsky, V. Bashtovoy, *Magnetic Fluids and Applications Handbook*, Begell House, Wallingford, NJ **1996**.
[31] C. H. Chang, C. W. Tan, J. M. Miao, G. Barbastathis, *Nanotechnology* **2009**, *20*, 4953011.
[32] G. Yang, B. F. Spencer, J. D. Carlson, M. K. Sain, *Eng. Struct.* **2002**, *24*, 309.
[33] P. Tartaj, M. D. Morales, S. Veintemillas-Verdaguer, T. Gonzalez-Carreno, C. J. Serna, *J. Phys. D: Appl. Phys.* **2003**, *36*, R182.
[34] A. K. Gupta, M. Gupta, *Biomaterials* **2005**, *26*, 3995.
[35] I. Brigger, C. Dubernet, P. Couvreur, *Adv. Drug Delivery Rev.* **2002**, *54*, 631.
[36] C. Fang, M. Q. Zhang, *J. Mater. Chem.* **2009**, *19*, 6258.
[37] D. A. LaVan, D. M. Lynn, R. Langer, *Nat. Rev. Drug Discovery* **2002**, *1*, 77.
[38] N. Xia, T. P. Hunt, B. T. Mayers, E. Alsberg, G. M. Whitesides, R. M. Westervelt, D. E. Ingber, *Biomed. Microdevices* **2006**, *8*, 299.
[39] A. K. Salem, P. C. Searson, K. W. Leong, *Nat. Mater.* **2003**, *2*, 668.
[40] D. H. Kim, E. A. Rozhkova, I. V. Ulasov, S. D. Bader, T. Rajh, M. S. Lesniak, V. Novosad, *Nat. Mater.* **2010**, *9*, 165.
[41] H. Masuda, M. Satoh, *Jpn. J. Appl. Phys., Part 2* **1996**, *35*, L126.
[42] F. Li, L. Zhang, R. M. Metzger, *Chem. Mater.* **1998**, *10*, 2470.
[43] J. Bachmann, R. Zierold, Y. T. Chong, R. Hauert, C. Sturm, R. Schmidt-Grund, B. Rheinländer, M. Grundmann, U. Gösele, K. Nielsch, *Angew. Chem. Int. Ed.* **2008**, *47*, 6177.
[44] J. Bachmann, J. Jing, M. Knez, S. Barth, H. Shen, S. Mathur, U. Gösele, K. Nielsch, *J. Am. Chem. Soc.* **2007**, *129*, 9554.
[45] K. Renger, *Ph.D. thesis*, University of Zurich **1913**.
[46] F. Walz, *J. Phys.: Condens. Matter* **2002**, *14*, R285.
[47] S. P. Sena, R. A. Lindley, H. J. Blythe, C. Sauer, M. Al-Kafarji, G. A. Gehring, *J. Magn. Magn. Mater.* **1997**, *176*, 111.
[48] D. Carlier, C. Terrier, C. Arm, J. P. Ansermet, *Electrochem. Solid-State Lett.* **2005**, *8*, C43.
[49] J. J. Crassous, R. Regisser, M. Ballauff, N. Willenbacher, *J. Rheol.* **2005**, *49*, 851.
[50] L. Kirschenmann, *Ph.D. thesis*, Ulm University **2003**.
[51] A. Bollero, M. Ziese, R. Höhne, H. C. Semmelhack, U. Köhler, A. Setser, P. Esquinazi, *J. Magn. Magn. Mater.* **2005**, *285*, 279.
[52] W. B. Mi, J. J. Shen, E. Y. Jiang, H. L. Bai, *Acta Mater.* **2007**, *55*, 1919.
[53] M. I. Shliomis, *Sov. Phys. JETP* **1972**, *34*, 1291.
[54] S. Odenbach, H. Störk, *J. Magn. Magn. Mater.* **1998**, *183*, 188.
[55] S. Odenbach, *Magnetoviscous Effects in Ferrofluids*, Springer, Berlin **2002**.